

Synthesis, experimental and theoretical characterization, and field-effect transistor properties of a new class of dibenzothiophene derivatives: From linear to cyclic architectures†

Yali Qiao,^a Zhongming Wei,^a Chad Risko,^b Hong Li,^b Jean-Luc Brédas,^{*bc} Wei Xu^{*a} and Daoben Zhu^{*a}

Received 15th August 2011, Accepted 21st October 2011

DOI: 10.1039/c1jm13962b

We report the synthesis and characterization of a bis-dibenzothiophene cyclic dimer containing bis-ethylene linkages (**DBT-CM**) and of the corresponding mono-ethylene-linked 'linear' *cis*- and *trans*-isomers (*cis*- and *trans*-**DBT-LM**, respectively). The varied molecular architectures lead to notable differences both in terms of the solid-state packing and the molecular electronic and optical properties. X-ray crystallography reveals that the cyclic architecture of **DBT-CM** leads to a more densely packed stacking configuration that imparts stronger intermolecular electronic coupling for both hole and electron transport amongst adjacent molecules, while characterization of the thin-film morphology and crystallinity uncovers important temperature-dependent properties of the films as a function of the molecular architecture. Moreover, the redox, electronic structure, and optical properties of **DBT-CM** vary distinctly from those of its linear counterparts. The intramolecular reorganization energies for hole and electron transport for **DBT-CM** are markedly smaller than the linear counterparts, while the dispersion for the highest valence band (and the intermolecular electronic coupling for hole transport) is the largest for the series. The more favorable molecular packing/morphology characteristics and charge-transport properties (within the Marcus framework) of **DBT-CM** manifest themselves in thin-film field-effect transistor studies, where a field-effect hole-carrier mobility $0.026 \text{ cm}^2 \text{ V}^{-1} \text{ s}^{-1}$ is measured, a value one-order-of-magnitude larger than either linear analog.

Introduction

First reported in 1986,¹ organic field-effect transistors (OFETs) still garner extensive academic and industrial attention^{2–7} as they offer a variety of advantages *versus* conventional inorganic silicon-based transistors – *e.g.*, relatively low-cost fabrication on large-area and flexible substrates – and show potential for use in a number of electronics applications, including radio frequency identification (RFID) tags, smart cards, and flexible displays.^{8–12} In order to fully take advantage of their inherent attributes in OFET applications, organic electronic materials should have

charge-carrier mobilities that are comparable to those of traditional amorphous silicon-based materials, around $1 \text{ cm}^2 \text{ V}^{-1} \text{ s}^{-1}$. Progress in terms of molecular design has led to a number of organic electronic materials possessing charge-carrier mobilities greater than that value being demonstrated.^{13–16} In spite of this progress, however, there remains a limited understanding of the relationship between molecular structure and electrical transport properties. Consequently, the design of new classes of organic electronic materials for OFET applications remains a challenging task.

Macrocyclic molecules with fully extended π -conjugation have been extensively studied in molecular materials chemistry, supramolecular chemistry, and nanotechnology applications.^{17–27} Compared to linear oligomers and polymers, cyclic π -conjugated compounds possess interesting characteristics that are principally attributed to their specific architecture, which effectively combines the well-defined structure of molecules/oligomers with the absence of end-effect perturbations (typical of the conjugated pathways of polymers).²⁸ Studies focused on the use of cyclic conjugated compounds in OFETs have been rather limited, though, as devices made from these materials have rather modest limited charge-carrier mobilities.^{29,30}

Recent investigations, however, reveal the potential for molecular systems based on cyclic architectures as promising

^aBeijing National Laboratory for Molecular Sciences, Key Laboratory of Organic Solids, Institute of Chemistry, Chinese Academy of Sciences, Beijing, 100080, P. R. China. E-mail: wxu@iccas.ac.cn; zhudb@iccas.ac.cn; Fax: +86 10 62569349; Tel: +86 10 62639355

^bSchool of Chemistry and Biochemistry and Center for Organic Photonics and Electronics, Georgia Institute of Technology, Atlanta, Georgia, 30332-0400, USA

^cDepartment of Chemistry, King Abdulaziz University, Jeddah, 21589, Saudi Arabia

† Electronic supplementary information (ESI) available: TGA data (Fig. S1), theoretical calculation data (Fig. S2, Table S1, S2, S3 and S4), AFM images for linear isomers (Fig. S3), NMR data (Fig. S4, S5, S6, S7 and S8), CCDC reference numbers 838083–838085. For ESI and crystallographic data in CIF or other electronic format see DOI: 10.1039/c1jm13962b

materials for OFETs.^{31–35} From a purely performance standpoint, OFETs based on Langmuir–Blodgett films of cyclo[8] pyrrole have large charge-carrier mobilities of $0.68 \text{ cm}^2 \text{ V}^{-1} \text{ s}^{-1}$, among the largest reported for cyclic π -conjugated compounds.³¹ Importantly, these expanded studies also allow for an improved understanding of the relationship between molecular structure and the charge-transport properties of cyclic architectures.^{33,35} For instance, materials based on cyclic triphenylamine dimers tested in OFET architectures have charge mobilities as large as $0.015 \text{ cm}^2 \text{ V}^{-1} \text{ s}^{-1}$ – among the best results for OFETs based on any triarylamine derivative and 100 times larger than that of the corresponding linear structure under the same conditions.³³ The nature of the cyclic architecture provides both for favorable, highly-ordered solid-state packing and a significant reduction in the intramolecular reorganization energy, both of which are major factors that facilitate efficient charge-carrier transport.

Dibenzothiophene (DBT) is a commercially available chalcogenophene compound with a planar π -conjugated structure, a feature desirable for inducing strong π – π intermolecular interactions. Additionally, the presence of sulfur in the conjugated backbone offers the potential for short S...S contacts that could provide additional channels for charge-carrier transport – e.g., various thiophene oligomers^{36,37} and tetrathiafulvalene derivatives³⁸ have lateral S...S interactions in the solid state that result in *interstack* electronic coupling (in addition to *intrastack* electronic coupling *via* π – π interactions), leading to two-dimensional charge-carrier pathways. If such multiple transport channels could be triggered in DBT-containing systems, it is anticipated that molecular structures with efficient charge-transport performance could be designed.

Linear oligomers based on DBT are known, and OFETs fabricated with these materials show promising performance,³⁹ however, macrocyclic DBT molecules have yet to be explored. Here, based on previous investigations on the synthesis of triphenylamine and carbazole dimers, we report the synthesis of a cyclic dibenzothiophene dimer bridged by two ethylene moieties (DBT-CM in Fig. 1). Both *cis*- and *trans*-mono-ethylene-linked ‘linear’ isomers (*cis*- and *trans*-DBT-LM in Fig. 1) were also synthesized for direct comparison with the cyclic dimer. The thermal, electrochemical, and optical properties were fully characterized, and single-crystal X-ray diffraction structures for all the three compounds were determined. OFET devices based

on vacuum-deposited films were successfully fabricated, and the results are discussed in terms of the thin-film morphology and crystallinity. OFETs based on cyclic DBT-CM display the largest hole mobility of $0.026 \text{ cm}^2 \text{ V}^{-1} \text{ s}^{-1}$, a value considerably larger than those obtained for the two linear isomers. The results suggest that cyclic DBT derivatives are interesting candidates that warrant further scrutiny for OFET applications.

Results and discussion

Synthesis and thermal characterization

The synthetic routes of the cyclic and linear dimers are presented in Scheme 1. For the cyclic compound DBT-CM, the synthetic strategy was the same as previously reported.^{33–35} Commercially available DBT was used as the starting material. DBT was brominated, followed by lithiation and reaction with DMF to afford 8-diformylbromobenzothiophene **2** in good yield. The cyclic macromolecule was then successfully obtained with the McMurry coupling reaction in much higher yields (16%) than previous attempts, which is mainly attributed to the use of 1,4-dioxane instead of THF as the reaction solvent.⁴⁰ For the linear dimers, the Wittig reaction was employed by using the precursors necessary to obtain both the *cis*- and *trans*-ethylene linear configurations. The compound *cis*-DBT-LM⁴² was initiated from dibenzothiophene, following a similar synthetic procedure to that mentioned above to produce 2-formyldibenzothiophene **4**.⁴³ Subsequently, compound **4** was reduced and reacted with triphenylphosphine hydrobromide to afford (dibenzothiophene-2-methyl)triphenylphosphonium bromide **6**.⁴⁴ Finally, the ethylene-bridged dimer *cis*-DBT-LM was successfully synthesized using the typical Wittig reaction in 39% yield. Other synthetic methods, for example, the McMurry reaction, were also used. However, difficulties with separation and purification

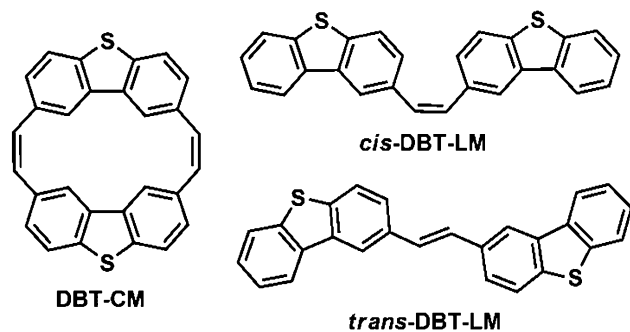
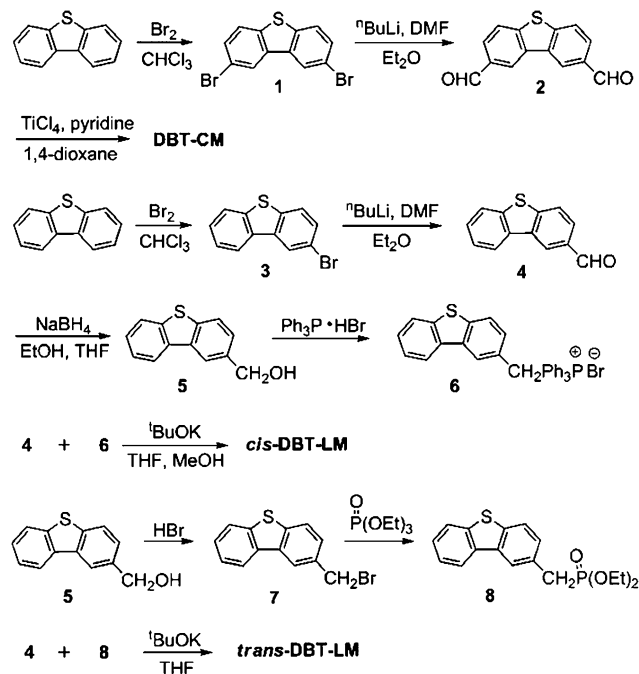


Fig. 1 Chemical structures of the cyclic and linear molecules: (*Z*, *Z*)-cyclo[2](dibenzo[*b,d*]thiophen-2-, 8-yl-ethylene) (DBT-CM), (*Z*)-1, 2-bis(dibenzo[*b,d*]thiophen-2-yl)ethane (*cis*-DBT-LM), (*E*)-1, 2-bis(dibenzo[*b,d*]thiophen-2-yl)ethene (*trans*-DBT-LM).



Scheme 1 Synthetic routes of the cyclic and linear molecules.

made the overall yields very low. Typical Wittig reaction conditions produced better results. In order to obtain the compound *trans*-DBT-LM, the precursor diethyl dibenzothio-phene-2-methylphosphonate **8** was synthesized from compound **6** through bromination and subsequent reaction with triethyl phosphate. Finally, the *trans*-isomer was synthesized with satisfactory yields (38%) using the improved Wittig reaction. Notably, for the synthesis of the two linear isomers, both *cis*- and *trans*-isomers are formed in each condensation reaction with different proportions, but only one, which is the most abundant, could be separated. Compounds DBT-CM and *cis*-DBT-LM were soluble in common organic solvents, such as dichloromethane and toluene, with a high solubility ($>10 \text{ mg mL}^{-1}$), but *trans*-DBT-LM had very low solubility in organic solvents ($<1 \text{ mg mL}^{-1}$ in chloroform or toluene at room temperature). All compounds were characterized by HRMS, NMR spectroscopy, and elemental analysis. Compound *trans*-DBT-LM could not be characterized by ^{13}C NMR spectroscopic analysis due to its poor solubility.

The thermal stability of the cyclic and linear isomers was investigated by thermal gravimetric analysis (TGA, see Fig. S1). The TGAs reveal that the onset thermal decomposition temperatures – determined from the intersection of the lines tangent to the isothermal mass-loss slope and initial base line – are approximately $275 \text{ }^\circ\text{C}$ for DBT-CM, $290 \text{ }^\circ\text{C}$ for the *cis*-isomer, and $345 \text{ }^\circ\text{C}$ for the *trans*-isomer under nitrogen atmosphere. These results indicate that the DBT-containing systems have good thermal stabilities.

Single crystal and molecular structures

Pale yellow, rod-like crystals of DBT-CM suitable for single-crystal X-ray diffraction structure analysis were grown by slow evaporation of the CH_2Cl_2 solution at room temperature. The cyclic molecule crystallizes in a monoclinic structure and belongs to the $P2_1/c$ space group with unit-cell parameters: $a = 12.339(3) \text{ \AA}$, $b = 4.748(9) \text{ \AA}$, $c = 16.949(3) \text{ \AA}$, $\beta = 110.06(3)^\circ$, see Fig. 2. Slipped face-to-face stacking columns along the b -axis are observed with an interplanar distance of 3.52 \AA between the thiophene rings of the stacked DBT units (Fig. 2b). There do exist relatively short $\text{S}\cdots\text{S}$ contacts with a distance of 3.48 \AA between neighboring columns (Fig. 2c), a distance smaller than twice the van der Waals radius of S atoms (3.70 \AA). The columns are linked through these short contacts into a two-dimensional layer in the a - b plane (Fig. 2c).

Colorless lamellar crystals of *cis*-DBT-LM suited for single-crystal X-ray diffraction structure analysis were obtained by slow evaporation of CH_2Cl_2 solution at room temperature. *cis*-DBT-LM crystallizes in a monoclinic system, space group $P2_1/c$, with the unit cell parameters of $a = 18.924(4) \text{ \AA}$, $b = 6.2925(13) \text{ \AA}$, $c = 7.9164(16) \text{ \AA}$, $\beta = 99.48(3)^\circ$, see Fig. 3. The *cis*-DBT-LM molecules stack in two dimensional layers along the b - c plane (Fig. 3b), with each layer containing two DBT moieties that come from neighboring *cis*-DBT-LM molecules (as the two DBT moieties in a particular molecule stack into separate layers). Within these layers, a herringbone packing pattern is observed (Fig. 3c).

As the solubility of the *trans*-isomer is poor in common solvents, crystals suitable for single-crystal X-ray diffraction

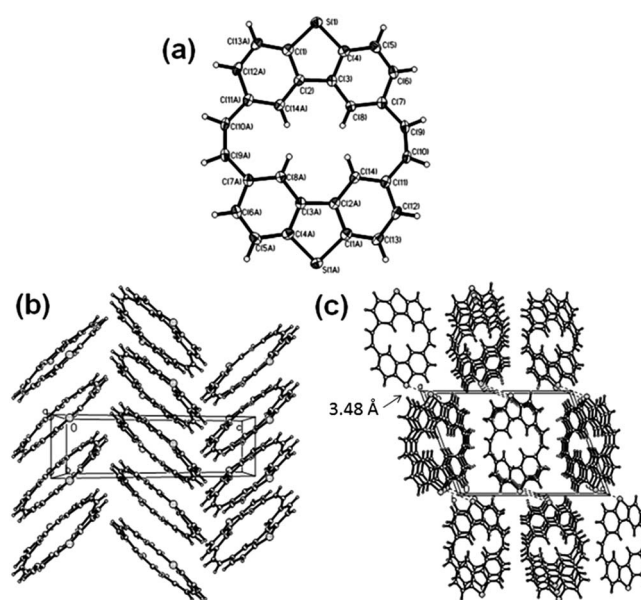


Fig. 2 X-ray crystal structure of compound DBT-CM: (a) Molecular structure with 50% probability ellipsoids. (b) Herringbone pattern viewed along the a -axis. (c) $\text{S}\cdots\text{S}$ short contacts viewed along the b -axis.

structure analysis could be obtained only by very slow evaporation of an extremely dilute CH_2Cl_2 solution. The *trans*-isomer crystallizes in a monoclinic system and belongs to the $P2_1/c$ space group with unit-cell parameters of $a = 6.792(15) \text{ \AA}$, $b = 10.677(2) \text{ \AA}$, $c = 12.729(3) \text{ \AA}$, $\beta = 97.719(4)^\circ$, see Fig. 4. In the packing diagram of *trans*-DBT-LM depicted in Fig. 4b, the molecules stack in columns along the a -axis in a slipped face-to-face manner. Close intermolecular packing is observed along the column as the interplanar distance is only 3.30 \AA (Fig. 4c). Furthermore, intermolecular $\text{S}\cdots\text{H}-\text{C}$ hydrogen bonds link these columns into a three-dimensional network.

Regardless of the molecular architecture, each molecular structure has a two-fold rotational axis, with the individual

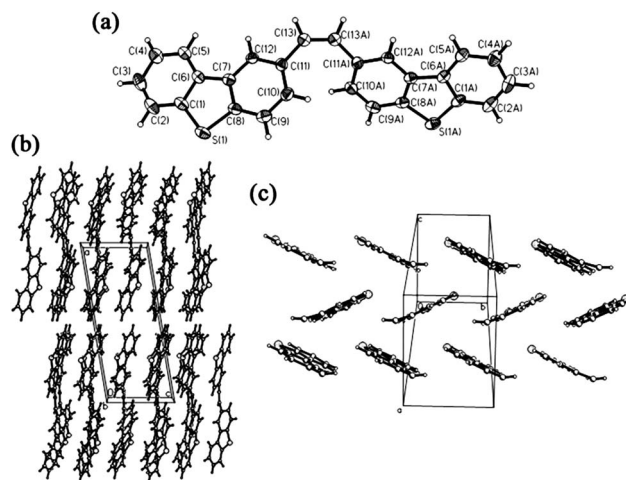


Fig. 3 X-ray crystal structure of compound *cis*-DBT-LM: (a) Molecular structure with 50% probability ellipsoids. (b) Layer stacking viewed along the b - c plane. (c) Herringbone pattern in one layer (one DBT moiety in each molecule was omitted for clarity).

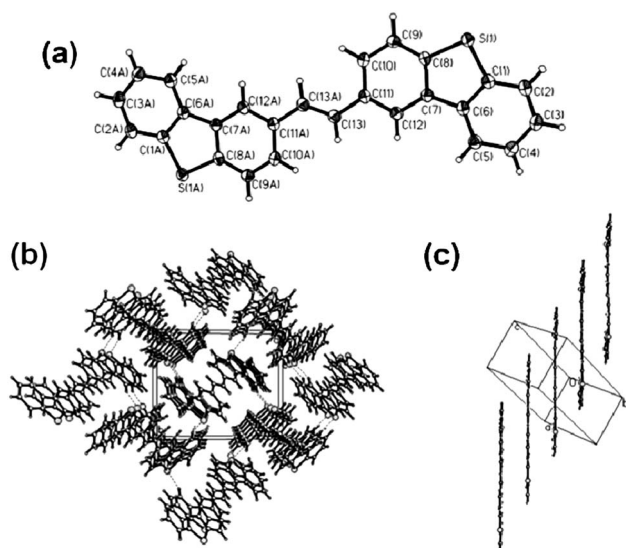


Fig. 4 X-ray crystal structure of compound *trans*-DBT-LM: (a) Molecular structure with 50% probability ellipsoids. (b) Column stacking viewed along *a*-axis. (c) π - π stacking in one column.

molecular symmetries being C_{2h} for **DBT-CM** and *trans*-**DBT-LM** and C_2 for *cis*-**DBT-LM**. Density functional theory (DFT) calculations of the neutral, ground-state structures were carried out to directly compare with those derived by X-ray crystallography; select DFT (B3LYP/6-31G**) -calculated geometric parameters for the neutral, radical-cation, and radical-anion states of **DBT-CM**, *cis*-**DBT-LM**, and *trans*-**DBT-LM** are given in Table S1 (bond numbering scheme shown in Fig. S2) and compared with crystallographic bond lengths. In general, there is good agreement between experiment and theory, with differences in carbon-carbon bond lengths for the various molecular structures of <0.01 Å; the largest deviation occurs for the description of the carbon-sulfur bonds, with the DFT results providing a slightly longer (by 0.015 Å–0.017 Å) bond length.

The presence of the bis-ethylene linkers and steric interactions between neighboring hydrogen atoms in **DBT-CM** induces considerable strain within the molecule as compared to its linear counterparts. As such, the ethylene bonds in **DBT-CM** are longer (1.352 Å/1.358 Å, X-ray/DFT) *versus* the linear systems (1.335 Å/1.350 Å for *cis*-**DBT-LM** and 1.334 Å/1.349 Å for *trans*-**DBT-LM**). The longer ethylene bond in the strained vinylene linkages in **DBT-CM** decreases the degree of bond-length alternation (BLA) within this segment *versus* the linear structures: 0.118 Å/0.113 Å (X-ray/DFT) for **DBT-CM**, 0.137 Å/0.124 Å for *cis*-**DBT-LM**, and 0.128 Å/0.116 Å for *trans*-**DBT-LM**.

Additional structural differences across the molecular series are induced due to the varying steric interactions caused by the modified bonding patterns about the ethylene linkers. First, the individual **DBT** units in the linear analogs are planar, while the **DBT** units in the more strained **DBT-CM** structure adopt a slightly curved geometry with bends (dihedral angle) of about 4.7° and 6.7° (7.1° for both sides, DFT) between the plane of the five-membered thiophene ring and the individual planes of the fused six-membered benzene rings. Moreover, the molecular structure of *trans*-**DBT-LM** displays a nearly coplanar geometry, while the **DBT** units in *cis*-**DBT-LM** and **DBT-CM** do not lie in

the same plane; the **DBT** units in **DBT-CM** are offset by a height of 1.4 Å (1.5 Å DFT, defined by the interplanar distances between the thiophene rings), while the dihedral angle about the ethylene bridge between the **DBT** units in *cis*-**DBT-LM** is 52.7° (52.3° DFT).

Redox properties

The empirical electrochemical and optical characteristics are summarized in Table 1. Cyclic voltammetry (CV) and differential pulse voltammetry (DPV) measurements were carried out on dichloromethane solutions of all three compounds and **DBT** (for reference) at room temperature. As shown in Fig. 5, the three dimer compounds present irreversible oxidative peaks, and no peaks along the negative potential sweep were observed to allow further analysis concerning the reduction process. The first oxidation onset for the cyclic, *cis*-, and *trans*-dimers are at 1.31 V, 1.25 V and 1.10 V, respectively; each of these is at considerably lower potential *versus* that for **DBT** (1.64 V). Within the CV profile for **DBT-CM**, other oxidation peaks appeared to be hidden within the broad feature, therefore DPV was used to delineate any further oxidation peaks. At least two definite oxidation peaks exist for each compound within the DPV sweep area. The first two oxidation peaks lie at 1.34 V and 1.50 V for **DBT-CM**, 1.26 V and 1.60 V for *cis*-**DBT-LM**, and 1.12 V and 1.58 V for *trans*-**DBT-LM**. Onset oxidation potentials from the DPV experiments are determined to be 1.25 V, 1.22 V, and 1.05 V for the cyclic, *cis*-, and *trans*-dimers, respectively, and 1.58 V for **DBT**, trends that are in good agreement with the CV-determined onsets. The solid-state ionization potential energy was estimated from the onset oxidation potential by using the relationship $IP^{ss} = -(4.40 + E_{ox}^{onset})eV$.⁴⁵ The IP^{ss} values are relatively large, on the order of 5.5–5.6 eV, which should indicate good stability against oxygen under ambient conditions.⁴⁶ However, such large IP^{ss} energies could be problematic with respect to OFET applications as they might lead to large hole-injection barriers (for example, the IP^{ss} of sexithienyl is 5.2 eV, which matches well with the work function of the Au electrode and thus provides for a much smaller hole-injection barrier).

Adiabatic/vertical ionization potential and electron affinity energies and HOMO and LUMO energies as determined at the B3LYP/6-31G(d,p) level are given in Table S2; data for **DBT** are provided for reference. The bridged dimer systems show a marked reduction in the ionization potential *versus* the parent **DBT** structure (>1 eV), a result in agreement with the electrochemical data. The calculated ionization potentials suggest that the cyclic and *trans*-linear forms are more easily oxidized than the *cis*-isomer, though the energetic differences are small. This differs slightly from the electrochemical analysis, which indicates that the *trans*-isomer is more readily oxidized than both the cyclic and *cis*-linear isomers (which are oxidized at nearly the same potential). The very limited potential/energetic ranges observed in the electrochemical/theoretical data (0.20 V range in electrochemical results and 0.11 eV range in the adiabatic ionization potentials) indicate that all three compounds are in fact oxidized at similar energies, with polarization effects from the solvent environment inducing slight changes to the relative order. The electron affinity energies indicate that the reduction of **DBT-CM** (-0.47 eV)

Table 1 Optical and electrochemical properties of cyclic and linear molecules

Compound	CV			DPV		UV-vis	
	$E_{\text{ox}}^{\text{onset}}$ [V] ^b	E_{ox}^1 [V] ^a	$E_{\text{ox}}^{\text{onset}}$ [V] ^b	IP ^{ss} [eV] ^c	E_{ox}^2 [V] ^a	Soln. ^d λ_{onset} [nm]	Film ^e λ_{onset} [nm]
DBT	1.64	1.81	1.58	5.98	–	334	–
DBT-CM	1.31	1.34	1.25	5.65	1.50	350	434
<i>cis</i> - DBT-LM	1.25	1.26	1.22	5.62	1.60	375	445
<i>trans</i> - DBT-LM	1.10	1.12	1.05	5.45	1.58	385	396

^a Calculated from the potential at peak of oxidation. ^b $E_{\text{ox}}^{\text{onset}}$ is the onset potentials for oxidation. ^c Calculated using the empirical equation: $\text{IP}^{\text{ss}} = -(4.40 + E_{\text{ox}}^{\text{onset}})$ eV. ^d Measurements performed in a dilute CH_2Cl_2 solution (1×10^{-5} M). ^e Measurements performed on vacuum-deposited film.

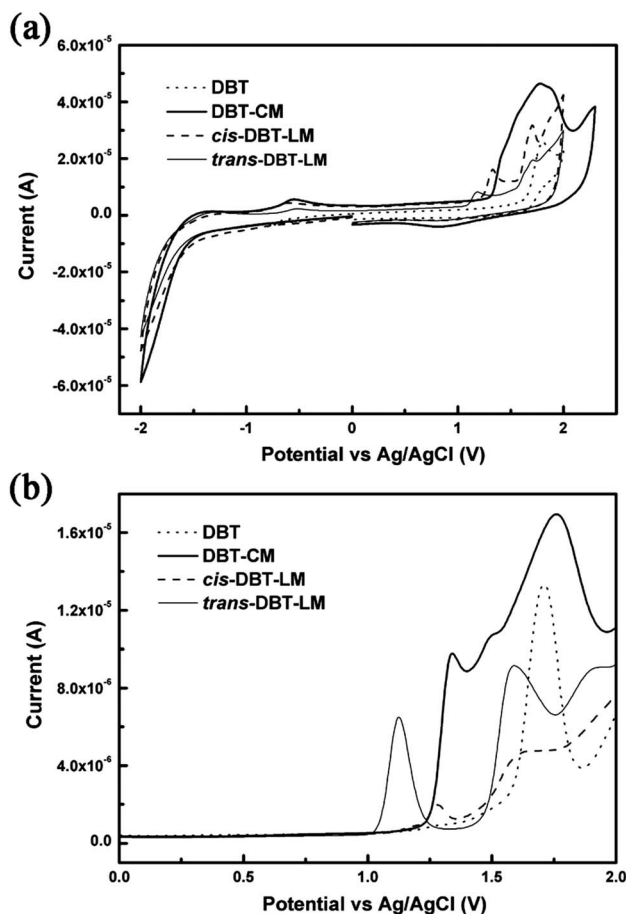


Fig. 5 (a) Cyclic voltammogram calibrated with ferrocene/ferrocenium (Fc/Fc^+) redox system as an external potential marker⁵⁵ and (b) differential pulse voltammetry of the cyclic and linear molecules in CH_2Cl_2 solution at room temperature.

should be somewhat easier than either linear system (-0.25 eV *cis*-**DBT-LM** and -0.32 eV *trans*-**DBT-LM**).

The oxidation and reduction processes lead to sizeable geometric changes for each molecule in the series, with the changes (while similar in nature) being more pronounced in the two linear structures. On oxidation to the radical-cation state, the most significant bond-length changes occur for the carbon–sulfur bond contained within the **DBT** moiety and the carbon–carbon bonds that comprise the full vinylene bridge, while the carbon–carbon bonds in the fused benzene rings undergo much

smaller changes. The carbon–sulfur bonds shorten by $\Delta = 0.017$ Å, 0.031 Å, and 0.030 Å in **DBT-CM**, *cis*-**DBT-LM**, *trans*-**DBT-LM**, respectively. A shortening of the single bond ($\Delta = 0.018$ Å, 0.037 Å, and 0.033 Å in **DBT-CM**, *cis*-**DBT-LM**, *trans*-**DBT-LM**, respectively) and lengthening of the double bond ($\Delta = 0.015$ Å, 0.032 Å, 0.029 Å in **DBT-CM**, *cis*-**DBT-LM**, *trans*-**DBT-LM**, respectively) in the vinylene bridge reduces considerably the BLA in the oxidized species (BLA = 0.080 Å, 0.055 Å, and 0.054 Å in **DBT-CM**, *cis*-**DBT-LM**, *trans*-**DBT-LM**, respectively). In **DBT-CM**, the interplanar distance between the thiophene rings increases slightly to 1.6 Å, while the dihedral angle between the **DBT** units in *cis*-**DBT-LM** closes substantially to 28.0° .

In contrast, there is minimal change to the carbon–sulfur bond length on reduction of **DBT-CM**, while the bond-length change in the linear analogs is reduced ($\Delta = 0.015$ Å in both *cis*-**DBT-LM**, *trans*-**DBT-LM**) versus oxidation. The bond-length changes to the vinylene bridges, however, are substantial. As with oxidation, the single bond shortens ($\Delta = 0.022$ Å, 0.041 Å, and 0.037 Å in **DBT-CM**, *cis*-**DBT-LM**, *trans*-**DBT-LM**, respectively) and the double bond lengthens ($\Delta = 0.025$ Å, 0.048 Å, 0.043 Å in **DBT-CM**, *cis*-**DBT-LM**, *trans*-**DBT-LM**, respectively). These geometric changes lead to a marked reduction in BLA for the reduced species (BLA = 0.066 Å, 0.035 Å, and 0.036 Å in **DBT-CM**, *cis*-**DBT-LM**, *trans*-**DBT-LM**, respectively). In **DBT-CM**, the interplanar distance between the thiophene rings decreases slightly to 1.4 Å, while the dihedral angle between the **DBT** units in *cis*-**DBT-LM** closes slightly to 45.6° .

Based on the adiabatic potential energy surfaces for the neutral and radical-ion states, the intramolecular reorganization energies for the oxidation and reduction processes were determined, see Table S3. The intramolecular reorganization energy combines the geometric relaxation energies of the electron-donor and of the electron-acceptor upon a charge-transfer reaction. For all three systems, the intramolecular reorganization energy for hole transport (λ_{h}) = 0.151 eV, 0.320 eV, and 0.228 eV in **DBT-CM**, *cis*-**DBT-LM**, *trans*-**DBT-LM**, respectively) is smaller than that for electron transport (λ_{e}) = 0.200 eV, 0.435 eV, and 0.265 eV in **DBT-CM**, *cis*-**DBT-LM**, *trans*-**DBT-LM**, respectively). Importantly, the intramolecular reorganization energies for both holes and electrons determined for the cyclic **DBT-CM** system are smaller (a function of the smaller bond length changes across the cyclic molecular structure both for oxidation and reduction) than those for the linear systems, a result consistent with previous studies of macrocyclic systems.⁴⁷ We note that the hole reorganization energy for **DBT-CM** is only slightly larger than that calculated for anthracene, 0.137 eV at the same level of

theory.⁴⁸ Between the linear configurations, the *trans*-configuration has smaller intramolecular reorganization energies for both charge carriers, a result that principally arises from the coplanarity of the **DBT** moieties in *trans*-**DBT-LM** and the sizeable changes to the dihedral angle between the **DBT** moieties in *cis*-**DBT-LM** on oxidation and reduction.

To further assess the nature of reorganization processes, the potential energy surfaces of the neutral and radical-ion states were expanded in a power series of the normal-mode coordinates to weigh the contribution of each vibrational mode to the individual relaxation processes. The relaxation energy, λ_r , can be expressed in terms of the harmonic approximation as

$$\lambda_r = \sum \lambda_i = \sum \hbar\omega_i S_i \quad (1)$$

$$\lambda_i = \frac{k_i}{2} \Delta Q_i^2, \quad S_i = \lambda_i / \hbar\omega \quad (2)$$

where S_i denotes the Huang-Rhys factor (electron-vibration coupling constant); ΔQ_i is the displacement along the normal mode i between the equilibrium position of the ground and radical-ion states; k_i and ω are the force constants and vibrational frequencies; and the summations run over all vibrational modes.^{9,49–53} For all three systems, the intramolecular reorganization energy for hole transport ($\lambda_t(h) = 0.151$ eV, 0.359 eV, and 0.229 eV in **DBT-CM**, *cis*-**DBT-LM**, *trans*-**DBT-LM**, respectively) and electron transport ($\lambda_t(e) = 0.199$ eV, 0.596 eV, and 0.274 eV in **DBT-CM**, *cis*-**DBT-LM**, *trans*-**DBT-LM**, respectively) is consistent with the picture derived by the analyses of the adiabatic potential energy surfaces (Table S3).

For holes, the intramolecular reorganization energy arises from a series of high-energy vibrations in the range of $1000 \approx 1600$ cm^{-1} and low-energy vibrations in the range of $100 \approx 600$ cm^{-1} , with one vibrational mode, in general, playing a predominant role in each region (Fig. 6). The principal high-energy vibrational mode for the radical-cation states (1614 cm^{-1} for **DBT-CM**; 1604 cm^{-1} for *cis*-**DBT-LM**; and 1577 cm^{-1} for *trans*-**DBT-LM**) can best be described as a carbon–carbon stretch coupled with a carbon–hydrogen rock that is centered on the bridging ethylene bond(s), with some additional carbon–carbon stretch behavior within the **DBT** moieties. This result is consistent with the substantial BLA changes on oxidation. The low-energy modes (412 cm^{-1} for **DBT-CM**; 18 cm^{-1} , 302 cm^{-1} , 396 cm^{-1} and 432 cm^{-1} for *cis*-**DBT-LM**; and 151 cm^{-1} for *trans*-**DBT-LM**) can primarily be described as breathing modes (coupled to other carbon–carbon, carbon–sulfur, and carbon–hydrogen motions) centered on the ethylene bridge(s) that move the independent **DBT** structures in concert with each other—a motion that is more pronounced in *cis*-**DBT-LM** and consistent with the large change in the dihedral angle about the vinylene bridge on oxidation.

A similar situation arises for electrons, though the high-energy modes contribute more significantly to the larger relaxation processes. For **DBT-CM** (1611 cm^{-1}) and *trans*-**DBT-LM** (1594 cm^{-1}), the ethylene-centered carbon–carbon stretch is the main mode of note; the contribution of this mode to the relaxation process nearly doubles in the radical-anion state *versus* that observed for the radical-cation, and is consistent with the larger bond-length changes in the vinylene linkage on reduction *versus*

oxidation. In the case of *cis*-**DBT-LM**, a number of low-energy modes – in particular similar dihedral/ring breathing modes at 19 cm^{-1} and 418 cm^{-1} – contribute along with a main high-energy mode (1573 cm^{-1} , a carbon–carbon stretch centered on the ethylene bridge) to the rather large reorganization of the system on reduction.

Optical properties

The UV-vis spectra of **DBT**, **DBT-CM**, *cis*-**DBT-LM**, and *trans*-**DBT-LM** in dilute CH_2Cl_2 solution are displayed in Fig. 7a, with each spectrum showing a number of features. **DBT** has three main absorption bands with the strongest absorption at 236 nm, and two weaker bands around 280 nm and 320 nm. Formation of the cyclic dimer **DBT-CM** leads to slightly red-shifted, broader absorption bands *versus* the **DBT** monomer, though one is able to distinguish three bands in the 220–350 nm region. The *cis*-isomer shows a very similar absorption profile, except that the bands are much broader and the relative intensity of the weaker bands at 300 nm and 320 nm increases significantly. With regard to the *trans*-isomer, the absorption peaks at longer wavelength (between 300 nm and 350 nm) continue to broaden, red-shift, and intensify *versus* the *cis*-isomer.

Fig. 7b–d shows a comparison of the (normalized) solution UV-vis spectra with those of vacuum-deposited thin films. The maximum absorbance of **DBT-CM** in thin films occurs at 265 nm, which is significantly red-shifted (20 nm, 0.38 eV), suggesting the possible formation of J-type aggregates in the solid state that lead to strong intermolecular interactions.⁵⁴ The existence of such strong interactions between adjacent molecules in the film is potentially favorable for achieving good OFET performance. The *cis*- and *trans*-isomers display similar trends to the cyclic compound in the solid state with the absorption peaks bathochromically shifted by 35 nm (0.65 eV) and 49 nm (0.48 eV), respectively.

Excited-state vertical transition energies (and wavelengths), oscillator strengths, and excited-state electronic configurations as determined with TDDFT at the B3LYP/6-31G** level of theory are given in Table S4. The TDDFT excitation energies for the first electronically-allowed transitions (4.01 eV, 3.71 eV, and 3.56 eV for **DBT-CM**, *cis*-**DBT-LM**, *trans*-**DBT-LM**, respectively) show similar trends to the excitation energy onsets in solution (3.54 eV, 3.30 eV, and 3.22 eV for **DBT-CM**, *cis*-**DBT-LM**, *trans*-**DBT-LM**, respectively), though the TDDFT results (that are obtained for isolated molecules) are blue-shifted with respect to experiment. For **DBT-CM**, a number of low-lying excited states have little-to-no transition dipole moment. This includes the first transition, the HOMO (B_u) \rightarrow LUMO (A_u) electronic excitation, which is symmetry forbidden due to the C_{2h} symmetry of the molecular structure. The first allowed transition occurs at 4.01 eV (310 nm), whose electronic configuration primarily includes electronic excitations from HOMO-1 \rightarrow LUMO (50%) and HOMO \rightarrow LUMO + 3 (24%). On the other hand, the *trans*-**DBT-LM** (3.56 eV and 3.78 eV) and *cis*-**DBT-LM** (3.71 eV and 3.81 eV) conformers have two, low-lying excited states that are close to each other energetically. In each case, the lowest-lying state is principally described as a HOMO \rightarrow LUMO electronic excitation, while the second transition is HOMO \rightarrow LUMO + 1 in the case of the *cis*-isomer and HOMO \rightarrow LUMO + 2 for the *trans*-isomer; even though *trans*-**DBT-LM** has the same C_{2h}

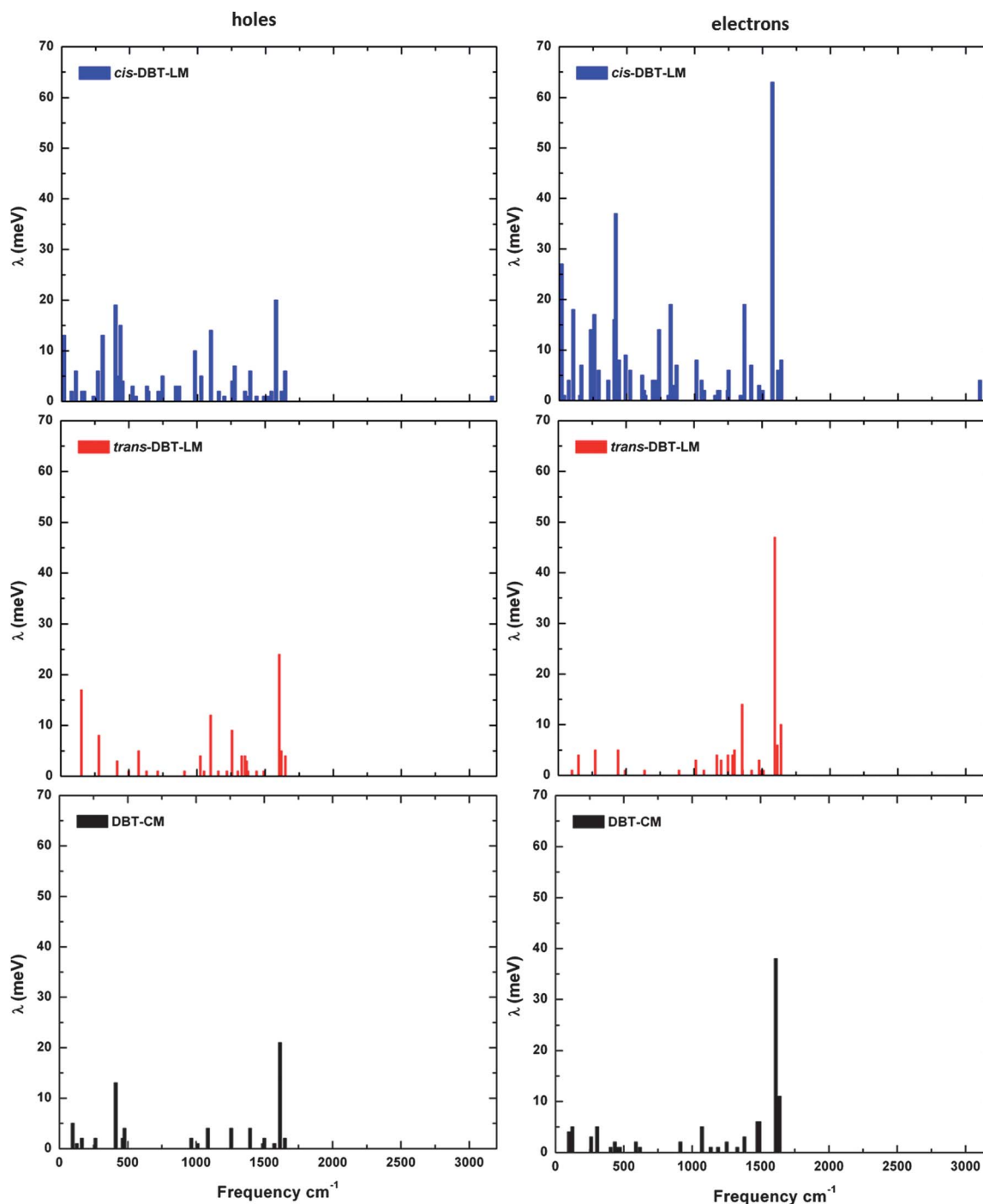


Fig. 6 Normal-mode contributions to the total intramolecular reorganization energy for holes (left) and electrons (right) as determined at the B3LYP/6-31G(d,p) level of theory.

symmetry representation as **DBT-CM**, the HOMO (A_u) \rightarrow LUMO (B_g) transition is electronically allowed and therefore observed.

Film morphology and characteristics

OFET device performance strongly depends on the morphology and crystallinity of the semiconductor thin films, both of which can be largely influenced by the temperature of the substrate on

which the material is deposited. Therefore, thin films of the cyclic molecule and the linear isomers deposited at different substrate temperatures were investigated by atomic force microscopy (AFM) and X-ray diffraction (XRD). Thin films of **DBT-CM** and *cis/trans*-**DBT-LM** with a thickness of 50 nm were fabricated by vacuum-deposition on OTS-treated SiO_2/Si substrates. As shown in the AFM images (Fig. 8), the thin-film morphology of **DBT-CM** undergoes obvious changes with increased substrate temperature. When the substrate is held at 15 °C, relatively

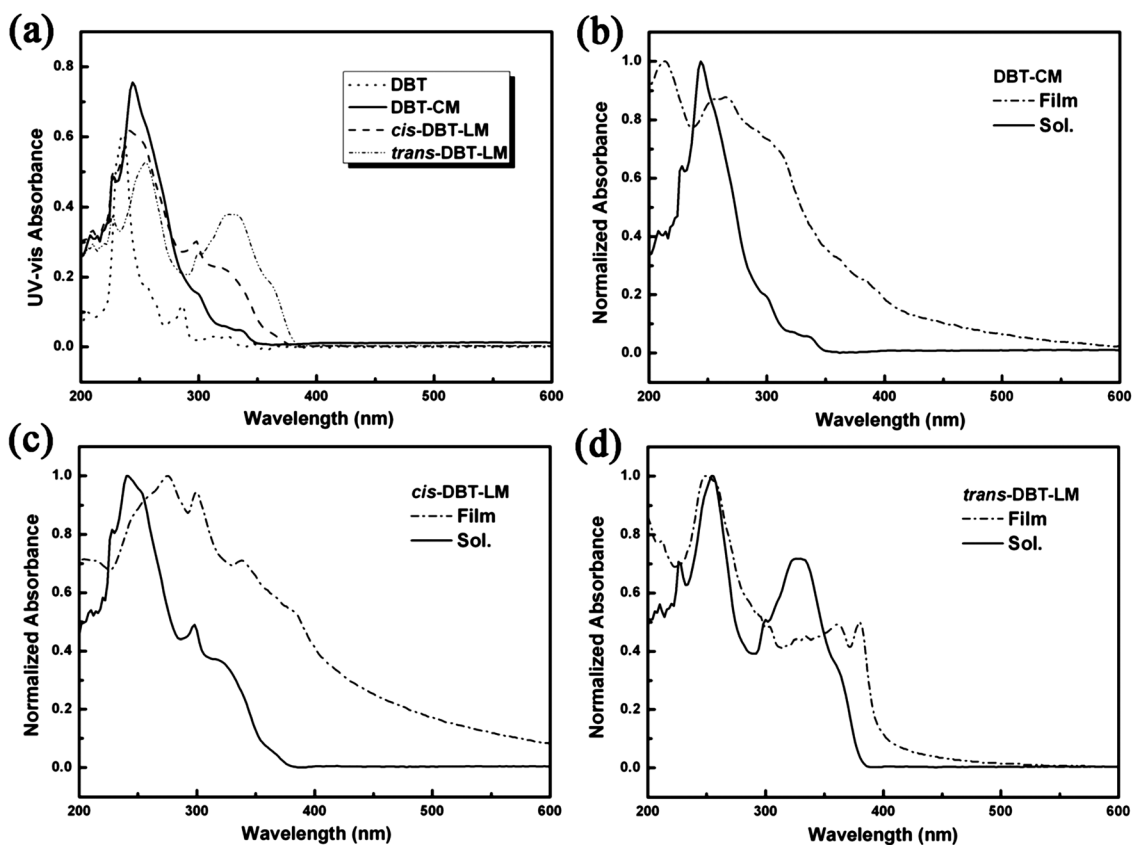


Fig. 7 UV-vis absorption spectra of (a) all the three target compounds and dibenzothiophene in dilute CH_2Cl_2 solution (1×10^{-5} M); (b) DBT-CM, (c) *cis*-DBT-LM, and (d) *trans*-DBT-LM in dilute CH_2Cl_2 solution (Sol.) and in the solid state (Film). Thin films with about 50 nm thickness were fabricated by a vacuum deposition method on quartz substrates at room temperature.

densely-packed, two-dimensional belt-like crystalline grains form with an average length of several micrometres. The good network interconnection between the crystallites might account for the larger charge-carrier mobilities observed for films deposited at this temperature (*vide infra*). With the substrate temperature held at 60 °C, the belt-like grains grow in size, leading to increased film discontinuity and intergrain boundaries. When the substrate temperature is brought to 100 °C, both the grain sizes and intergrain gaps increase, a result that is expected to have a negative effect on OFET performance.

The crystallinity and molecular orientation of the thin films were also analyzed by XRD (Fig. 8). At 15 °C, the first peak appears at 8.8° with a *d*-spacing of 10.0 Å, corresponding to the thickness of a molecular monolayer. The molecular orientation on the substrate can be estimated by comparing the monolayer thickness with the actual molecular length; according to the molecular height (10.4 Å) derived from single crystal data, it is estimated that the molecules exhibit end-to-end packing on the substrate, resulting in an almost perpendicular arrangement of cyclic molecules on the dielectric surface. A relatively weak peak at 17.6° with a *d*-spacing of 5.0 Å is the second-order reflection peak, whereas a much weaker peak at 11.7° is caused by a tilted arrangement, rather than multiple orders of the dominant peak. When the substrate temperature is increased to 60 °C, the peak in the 11–12° region disappears and the intensity of the two remaining major peaks increases, indicating an increased

crystallinity in the film. However, the film shows less continuity and larger grain boundaries at the same time, which results in a decrease in OFET performance (*vide infra*). Raising the substrate temperature to 100 °C leads to a further reduction in the peak intensities.

The AFM and XRD analyses of the thin films of the two linear isomers at room temperature are displayed in Fig. 9. For the *cis*-isomer, the AFM image reveals small grains and a discontinuous film. The film of the *trans*-isomer shows a similar morphology with much smaller grains; however, several strong reflection peaks are observed in the XRD analysis, indicative of the formation of a more polycrystalline film. The results are consistent with the fact that the *trans*-isomer shows slightly better performance in OFET devices than the *cis*-isomer, though the charge-carrier mobilities for both systems are one order of magnitude lower than that of the cyclic macromolecule (*vide infra*).

OFET measurements and charge mobility

OFET devices were fabricated and measured in a top-contact configuration, where the drain and source electrodes are deposited on top of the active layer. Thin films of 50 nm thickness were evaporated on OTS-modified SiO_2/Si substrates and gold electrodes were deposited subsequently by vacuum evaporation on the active layers through a shadow mask. The cyclic molecule

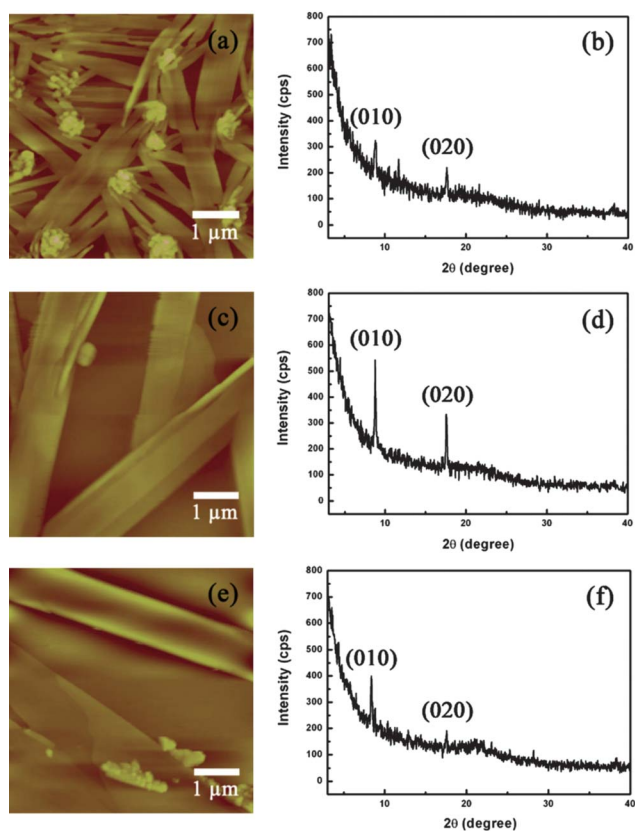


Fig. 8 AFM images and XRD patterns of 50-nm-thick thin films of compound **DBT-CM** vacuum deposited on OTS treated SiO₂/Si substrates at different temperatures: (a) and (b) T_{sub} at 15 °C; (c) and (d) T_{sub} at 60 °C; (e) and (f) T_{sub} at 100 °C. The scale of each AFM image is 5 μm × 5 μm.

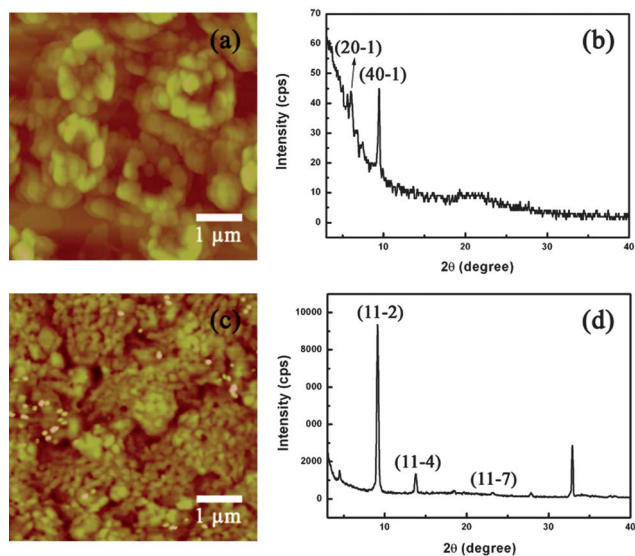


Fig. 9 AFM images and XRD patterns of 50-nm-thick thin films vacuum deposited on OTS treated SiO₂/Si substrates at room temperatures: (a) and (b) for *cis*-DBT-LM; (c) and (d) for *trans*-DBT-LM. The scale of each AFM image is 5 μm × 5 μm.

and linear isomers each exhibit p-type semiconductor characteristics in OFET devices. The OFET devices for the three compounds were tested at room temperature in air. The mobilities in the saturation regime from the gate sweep were determined using eqn (3):

$$I_D = (\mu_{FET} C_i W / 2L) (V_G - V_T)^2 \quad (3)$$

where I_D denotes the drain-source current in the saturated regime; (μ_{FET} , the field-effect transistor (FET) mobility; C_i , the capacitance of the gate dielectric layer; W and L , the channel width and length; V_G , the gate voltage; and V_T , the threshold voltage. OFET characteristics for the three compounds, with varying substrate deposition temperatures, are summarized in Table 2.

OFET performance is found to be closely related to the substrate temperature. In general, **DBT-CM** exhibits better overall device performance *versus* the two linear isomers under the same experimental conditions. For **DBT-CM**, the best OFET performance is obtained at room temperature with a charge-carrier mobility as high as 0.026 cm² V⁻¹ s⁻¹ and an on/off ratio of 10⁵. The output and transfer characteristics of a typical OFET device for **DBT-CM** deposited at 15 °C are provided in Fig. 10. The results are consistent with the AFM images that show formation of a continuous polycrystalline film with relatively densely-packed, two-dimensional belt-like crystalline grains. With the substrate temperature at 60 °C, the mobility decreases by an order of magnitude; this can be attributed to the observed film discontinuity and the formation of large intergrain gaps, even though XRD indicates an increase in the crystallinity. When the substrate temperature increases further to 100 °C, the mobility of **DBT-CM** decreases, which is possibly due to the much larger intergrain boundaries.

The performance of the two linear isomers is significantly worse under the same device fabrication and measurement conditions, consistent with previous results for triphenylamine and carbazole dimers with cyclic and linear architectures.^{31,34} When the substrate temperature increases to 60 °C, the grain sizes and boundaries of the thin films of *cis*- and *trans*-isomers become considerably larger (see Fig. S3); consequently, these highly discontinuous films show no field-effect properties.

Based on the crystal structures of **DBT-CM**, *trans*-**DBT-LM**, and *cis*-**DBT-LM**, the electronic band structures (Fig. 11) were calculated along a few high-symmetry directions in reciprocal space to provide a description of the hole-transport properties.

The intermolecular electronic couplings (transfer integrals) – indicators of the extent of wave-function overlap between pairs of molecules in the crystal – were also evaluated for holes using

Table 2 OFET characteristics of devices based on the three compounds fabricated under different substrate temperatures (°C)

Compound	T_{sub} [°C]	μ [cm ² V ⁻¹ s ⁻¹]	I_{on}/I_{off}	V_{th} [V]
DBT-CM	15	2.6×10^{-2}	10 ⁵	-43.9
	60	4.8×10^{-3}	10 ⁶	-51.1
	100	2.7×10^{-3}	10 ⁵	-53.9
<i>cis</i> - DBT-LM	15	1.5×10^{-3}	10 ⁶	-51.7
	60	–	–	–
<i>trans</i> - DBT-LM	20	6.6×10^{-3}	10 ⁵	-55.4
	60	–	–	–

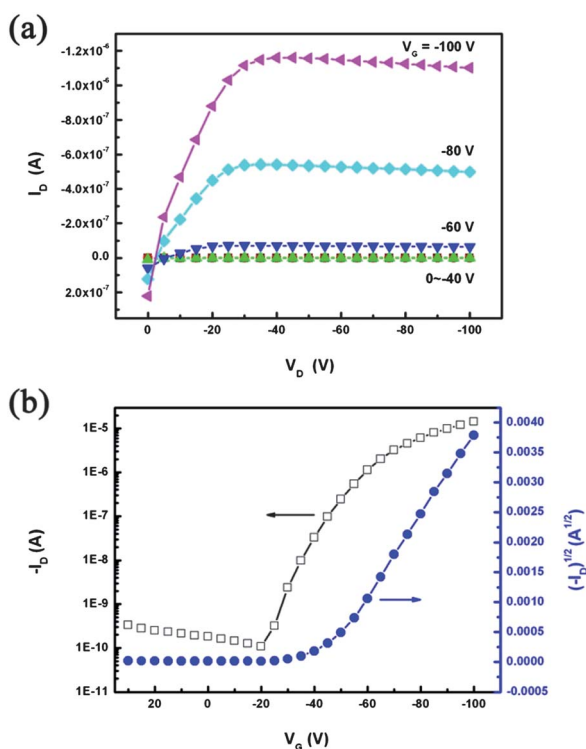


Fig. 10 OFET characteristics for devices based on **DBT-CM** OTS-modified SiO_2/Si substrate at room temperature: (a) output curve at different gate voltages; (b) transfer curve in the saturated regime at a constant source-drain voltage of -100 V and square root of the absolute value of the current as a function of the gate voltage.

the fragment orbital approach⁵² at the B3LYP/6-31G** level of theory, see Fig. 12 and Table 3. For **DBT-CM**, the conduction band (CB) minimum is found at the Γ -point, while the valence band (VB) maximum is close to the Z-point with a k -vector of $(0, 0.4559, 0)$; these results indicate the presence of an indirect band gap. Large dispersions for the highest VB (235 meV) are observed along the ΓZ direction, which corresponds to a direction associated with the b -axis in the crystal structure (the primary stacking direction of the **DBT-CM**

molecule). The effective mass for hole transport along the ΓZ direction (b -axis) is $3.0 m_0$. The computed HOMO–HOMO (70 meV) transfer integral between molecules denoted 2 and 3 in the **DBT-CM** unit cell (stacked along the b -axis, see Fig. 12) are fairly significant, as the prototypical organic semiconductor pentacene has a calculated transfer integral for holes of approximately 100 meV. We note that the highest VB width is only slightly smaller than four times the transfer integral, showing good correlation in the context of the tight-binding approximation. The band dispersion within the a – c plane (along the a^* - and c^* -directions) is very flat (not shown), a result in agreement with the minimal electronic couplings calculated for molecule pairs 1–2 and 1–3. Even though there exist short S··S contact distances between neighboring columns (that are smaller than twice the van der Waals radius of S atoms), the electronic coupling is calculated to be very small, indicating that interstack charge-transfer pathways through S··S contacts are modest at best in this system.

The band structure of *cis*-**DBT-LM** shows that the CB minimum is located at $(k = 0, 0.3375, 0)$ and the VB maximum is at the Γ point, indicating that *cis*-**DBT-LM** is also an indirect band-gap semiconductor. The smallest effective mass for hole transport

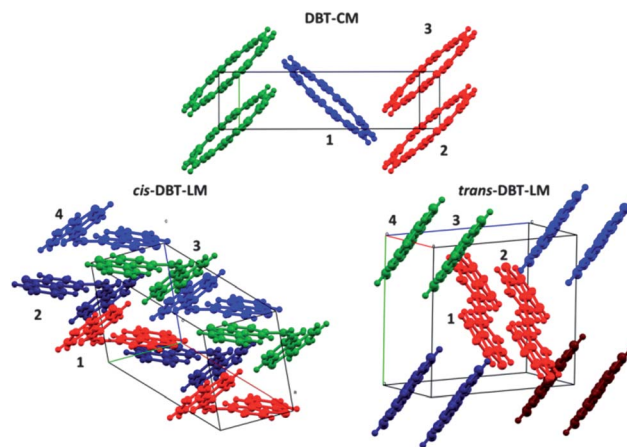


Fig. 12 Select electronic coupling pathways as determined from the crystal structure.

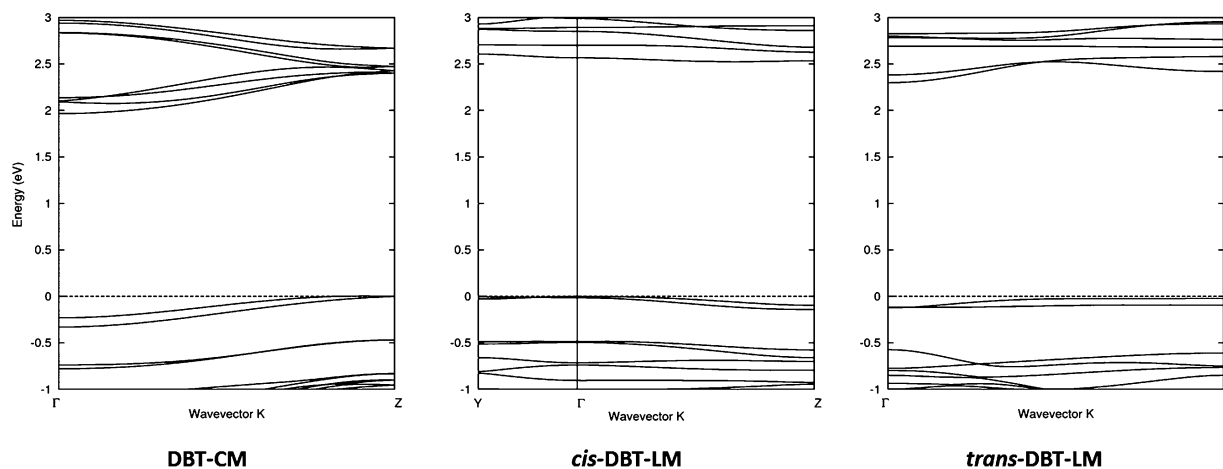


Fig. 11 Electronic band structures for the three compounds determined with the PW91 functional and ultra-soft pseudopotentials. For all the three crystal structures, ΓZ direction is along the b -axis of the crystal structure, ΓY is along the direction perpendicular to the c -axis within the a – c -plane of the crystal structure.

Table 3 Hole (HOMO-HOMO) electronic coupling (H_{ij} , meV) between adjacent molecules (see labeling in Fig. 12) for the three compounds as determined at the B3LYP/6-31G(d,p) level of theory

	H_{12}	H_{13}	H_{23}
DBT-CM	4	4	70
<i>cis</i> - DBT-LM	15	–	31
<i>trans</i> - DBT-LM	26	5	–

is $2.1 m_0$, along a path nearly aligned with the a -axis. The effective mass for holes is smaller than in the **DBT-CM** crystal, a result that is attributed to the strong intramolecular coupling between the two **DBT** fragments within the linear isomer. However, the transfer integrals for holes are small (15 meV–30 meV), principally due to the ‘V-shape’ of *cis*-**DBT-LM** that severely limits the intermolecular electronic coupling within the crystal. For *trans*-**DBT-LM**, the band dispersion for the two top valence bands is virtually flat along the selected high-symmetry directions. The VB maximum is found at the Y -point ($k = 0.5, 0, 0$), where the highest VB shows no dispersion; the intermolecular electronic coupling for hole transport is also determined to be small (26 meV).

Conclusion

Three dibenzothiophene dimers have been synthesized by McMurry coupling and Wittig reactions, including one cyclic molecule (**DBT-CM**) and two linear compounds (*cis*- and *trans*-**DBM-LM**). The structures were thoroughly characterized by means of NMR, HRMS, elemental analysis, electrochemistry, absorption spectroscopy, quantum-chemical analysis, and employed as the active materials in organic TFTs. The cyclic architecture affects significantly the molecular stacking pattern in the crystals, as well as the molecular and crystal electronic properties.

Several prominent reasons related to the cyclic architecture appear to contribute to the large mobility differences between the cyclic and linear compounds. First, the cyclic structure significantly improves the molecular ordering within the crystal, leading to larger band dispersions (and intermolecular electronic couplings) for hole transport. The better packing arrangements also lead to the formation of relatively densely-packed, two-dimensional belt-like crystalline grains with fine continuity. Even though smaller grains were obtained for the linear compounds, the denser packing motif of the cyclic structure leads to better charge-carrier mobility through the film. Moreover, the cyclic structure leads to a marked reduction in intramolecular reorganization energy for hole transport *versus* the linear isomers, a feature that aids in the improved hole-transport characteristics. Each of these characteristics leads to OFET devices based on **DBT-CM** having the largest charge-carrier mobility of $0.026 \text{ cm}^2 \text{ V}^{-1} \text{ s}^{-1}$, a one-order-of-magnitude improvement over either linear analog.

Experimental section

Synthesis

All reagents and solvents were purchased from commercial suppliers and used directly as received unless otherwise stated. Anhydrous diethyl ether, THF and 1,4-dioxane were distilled over Na/benzophenone. Pyridine was distilled over NaOH. DMF

and CH_2Cl_2 were dried and distilled over CaH_2 . Conventional Schlenk techniques were adopted and reactions were carried out under a nitrogen atmosphere unless otherwise stated. 2,8-Dibromodibenzothiophene (**1**), 2,8-diformyldibenzothiophene (**2**), 2-bromodibenzothiophene (**3**), 2-formyldibenzothiophene (**4**), 2-hydroxymethyldibenzothiophene (**5**) and (dibenzothiophene-2-methyl)triphenylphosphonium bromide (**6**) were synthesized according to literature procedures.^{40–44}

(*Z, Z*)-cyclo[2]([dibenzo[b,d]thiophen-2, 8-yl-ethylene) (**DBT-CM**)

Zn powder (5.43 g, 83 mmol) was suspended in 1,4-dioxane (300 mL) under N_2 . A solution of TiCl_4 (9.2 mL, 83 mmol) in 1,4-dioxane (50 mL) was added carefully to the suspension with stirring and then the suspension was heated to reflux at 130°C for 1 h. A solution of **2'** (1 g, 4.2 mmol) and pyridine (5.4 mL, 66 mmol) in 1,4-dioxane (150 mL) was added dropwise to the reaction mixture. The mixture was stirred and heated at reflux for 10 h, and after cooling to room temperature, saturated aqueous NaHCO_3 (200 mL) was added and the reaction mixture was stirred for an additional 0.5 h. The reaction mixture was filtered and most of the filtrate was removed under reduced pressure. The residual mixture was extracted with dichloromethane ($3 \times 100 \text{ mL}$) and the combined organic extracts were dried over anhydrous sodium sulfate, filtered, and concentrated under reduced pressure. The residue was purified by flash chromatography on silica gel using petroleum ether as the eluent to afford the crude product. Recrystallization from dichloromethane gave a yellow crystal (0.28 g, 16%). M.P. 310°C ; $^1\text{H NMR}$ (400 MHz, DMSO) δ 9.33 (s, 4H), 7.83–7.81 (d, $J = 8.3 \text{ Hz}$, 4H), 7.33–7.31 (d, $J = 8.3 \text{ Hz}$, 4H), 7.25 (s, 4H); $^{13}\text{C NMR}$ (100 MHz, CDCl_3) δ 138.7, 134.7, 132.6, 132.2, 127.7, 123.1, 122.2; EI-MS: $m/z = 416 [\text{M}]^+$; HRMS (GCT-MS): calculated for $\text{C}_{28}\text{H}_{16}\text{S}_2$: 416.0693; found: 416.0698 [$\text{M}]^+$; elemental analysis calculated (%) for $\text{C}_{28}\text{H}_{16}\text{S}_2$: C 80.73, H 3.87; found: C 81.01, H 3.73.

(*Z*)-1,2-bis(dibenzo[b,d]thiophen-2-yl)ethene (*cis*-**DBT-LM**)

To a solution of 2-formyldibenzothiophene (0.106 g, 0.5 mmol) and (dibenzothiophene-2-methyl)triphenylphosphonium bromide (0.27 g, 0.5 mmol) in THF/MeOH (6 mL, 2 : 1), tBuOK (0.112 g, 1 mmol) was added slowly. The resulting mixture was stirred at room temperature for 6 h. Water (10 mL) was added and the solution was extracted with chloroform ($3 \times 15 \text{ mL}$). The combined extracts were dried with Na_2SO_4 , and purified by chromatography using petroleum as the eluent on a short column to give a white powder (0.03 g, 39%). M.p. 185°C ; $^1\text{H NMR}$ (400 MHz, CDCl_3) δ 8.12 (s, 2H), 7.97 (d, $J = 7.6 \text{ Hz}$, 2H), 7.84 (d, $J = 7.7 \text{ Hz}$, 2H), 7.67 (d, $J = 8.3 \text{ Hz}$, 2H), 7.45–7.37 (m, 6H), 6.85 (s, 2H); $^{13}\text{C NMR}$ (100 MHz, CDCl_3) δ 139.9, 138.5, 135.9, 135.5, 133.8, 130.3, 127.8, 126.9, 124.6, 123.0, 122.6, 122.1, 121.7; EI-MS: $m/z = 392 [\text{M}]^+$; HRMS (GCT-MS): calculated for $\text{C}_{26}\text{H}_{16}\text{S}_2$: 392.0693; found: 392.0700 [$\text{M}]^+$.

(*E*)-1,2-bis(dibenzo[b,d]thiophen-2-yl)ethene (*trans*-**DBT-LM**)

To a solution of 2-formyldibenzothiophene (0.76 g, 3.59 mmol) and diethyl dibenzothiophene-2-methylphosphonate (1.13 g, 3.37 mmol) in THF (100 mL), tBuOK (0.73 g, 6.47 mmol) was added slowly. The resulting suspension was stirred at room

temperature overnight, followed by filtration to afford a light yellow powder that was then washed with water several times and further purified by recrystallization in toluene to provide white floccules (0.50 g, 38%). M.P. 281 °C; ^1H NMR (400 MHz, CDCl_3) δ 8.32(s, 2H), 8.24(d, $J = 8.1$ Hz, 2H), 7.87(d, $J = 8.1$ Hz, 4H), 7.72(d, $J = 8.3$ Hz, 2H), 7.51–7.49(m, 4H), 7.42(s, 2H); EI-MS: $m/z = 392$ [M] $^+$; HRMS (GCT-MS): calculated for $\text{C}_{26}\text{H}_{16}\text{S}_2$: 392.0693; found: 392.0699 [M] $^+$; elemental analysis calculated (%) for $\text{C}_{26}\text{H}_{16}\text{S}_2$: C 79.55, H 4.11; found: C 79.67, H 4.35.

Measurements and characterization

Melting points were measured on a BÜCHI Melting Point B-500. ^1H NMR and ^{13}C NMR spectra were performed on Bruker Advance 400 MHz spectrometers. MS (EI) measurements were performed on SHIMADZU GCMSQP2010 or UK GCT-Micromass spectrometers. HRMS (GCT-MS) measurements were performed on a Bruker APEX II FTICRMS spectrometer. Elemental analyses were measured on a Carlo Erba 1106 elemental analyzer.

UV-vis spectra were recorded on a JASCO V-570 spectrometer. Cyclic voltammetry (CV) measurements were carried out on a CHI660C analyzer in a conventional three-electrode cell setup with a platinum rod as the working electrode, a platinum wire as the counter electrode, Ag/AgCl as the reference electrode and calibrated with ferrocene/ferrocenium (Fc/Fc^+) as an external potential marker⁵⁵ in anhydrous CH_2Cl_2 solution containing 0.1 M $n\text{-Bu}_4\text{NPF}_6$ as a supporting electrolyte at a scan rate of 100 mVs^{-1} under a nitrogen atmosphere at room temperature. Differential pulse voltammetry (DPV) was also performed on a CHI660C analyzer in the same conventional three-electrode cell setup aforementioned (without any potential marker) at a pulse width of 0.05 s in a pulse period of 0.2 s with a sensitivity of 1×10^{-5} under a nitrogen atmosphere at room temperature. Thermogravimetric analysis (TGA) was performed on a Shimadzu DTG 60 instrument at a heating rate of $10^\circ\text{C min}^{-1}$ under a nitrogen atmosphere with runs recorded from room temperature to 550°C .

XRD measurements of thin films were performed in reflection mode at 40 kV and 200 mA with Cu-K α radiation using a 2 kW Rigaku X-ray diffractometer. AFM images of the thin films were obtained on a Nanoscope IIIa AFM (Digital Instruments) operating in tapping mode.

Single-crystal structure determination

X-ray crystallographic data were collected with a Bruker Smart CCD diffractometer through using graphite-monochromated Mo-K α radiation ($\lambda = 0.71073$ Å). The data were collected at 113 K and 173 K for the cyclic and two linear isomers, respectively. The structures were resolved by the direct method and refined by full-matrix least-squares on F^2 using the SHELXL-97 program.⁵⁶ All non-hydrogen atoms were refined anisotropically. Complete crystallographic data for the three compounds are available.†

Crystallographic data for DCM-CM. Crystal size: $0.18 \times 0.12 \times 0.10$ mm 3 ; monoclinic; P 2 $_1$ /c; Z = 2; $a = 12.339(3)$ Å, $b = 4.748(9)$ Å, $c = 16.949(3)$ Å; $V = 929.8(3)$ Å 3 ; $\rho_{\text{calculated}} = 1.483$ g cm $^{-3}$;

of 8817 reflections, 1550 were unique; GOF = 1.037; 136 parameters; $R_1 = 0.0352$, $wR_2 = 0.0905$ (for all reflections).

Crystallographic data for cis-DCM-LM. $0.10 \times 0.10 \times 0.02$ mm 3 ; monoclinic; P 2 $_1$ /c; Z = 2; $a = 18.924(4)$ Å, $b = 6.2925(13)$ Å, $c = 7.9164(16)$ Å; $V = 932.7(3)$ Å 3 ; $\rho_{\text{calculated}} = 1.402$ g cm $^{-3}$; of 7994 reflections, 1775 were unique; GOF = 1.159; 136 parameters; $R_1 = 0.0879$, $wR_2 = 0.1423$ (for all reflections).

Crystallographic data for trans-DCM-LM. $0.31 \times 0.10 \times 0.10$ mm 3 ; monoclinic; P 2 $_1$ /c; Z = 2; $a = 6.792(15)$ Å, $b = 10.677(2)$ Å, $c = 12.729(3)$ Å; $V = 914.8(4)$ Å 3 ; $\rho_{\text{calculated}} = 1.425$ g cm $^{-3}$; of 11960 reflections, 2007 were unique; GOF = 1.234; 136 parameters; $R_1 = 0.0660$, $wR_2 = 0.1176$ (for all reflections).

FET device fabrication and measurement

OFETs based on vacuum-deposited thin films were fabricated in a top-contact device configuration. A heavily doped n-type Si wafer with a 500 nm-thick SiO_2 layer and a capacitance of 7.5 nF cm $^{-2}$ was used as the substrate. The gate dielectric was treated with octadecyltrichlorosilane (OTS) by a vapor deposition method. All three materials were deposited on substrates by thermal evaporation under a pressure of $4\text{--}6 \times 10^{-4}$ Pa at a deposition rate gradually increased from 0.1 Å s $^{-1}$ to 0.5 Å s $^{-1}$ for the first 10 nm and then maintained until the thickness of the film was 50 nm. The deposition rate and film thickness were monitored by ULVAC CRTM-6000. Subsequently, 20 nm thick gold source and drain electrodes were deposited on the films *via* a shadow mask. The channel length and width were 0.11 mm and 5.30 mm, respectively. The FET characteristics were measured at room temperature in air using Keithley 4200 SCS.

Computational methodology

Analyses of the neutral ground-state and radical-ion structures for the cyclic and linear molecules were carried out using density functional theory (DFT). The B3LYP functional^{57–59} was used in conjunction with the 6-31G(d,p) basis set. Time-dependent DFT (TDDFT) calculations were employed to analyze the vertical transition energies, oscillator strengths, and electronic configurations for low-lying singlet excited states. All calculations were performed with Gaussian 09 (Revision A.02),⁶⁰ and molecular orbital density plots were generated with ArgusLab 4.0.1.⁶¹ Band-structure calculations at the DFT level were carried out using the Vienna Ab Initio Simulation Package (VASP)⁶² with ultra-soft pseudopotentials and the GGA exchange and correlation functional of Perdew and Wang (PW91).⁶³ A plane wave cut-off of 400 eV and a total energy convergence of 10^{-6} eV for the self-consistent iterations were applied in the calculations.

Acknowledgements

The authors are grateful to financial support from Solvay S. A., the National Natural Science Foundation of China, the State Key Basic Research Program, and the Chinese Academy of Sciences. The authors would like to thank Dr Stephen Barlow and Dr Veaceslav Coropceanu for fruitful discussions.

Notes and references

- 1 A. Tsumura, H. Koezuka and T. Ando, *Appl. Phys. Lett.*, 1986, **49**, 1210.
- 2 C. D. Dimitrakopoulos and P. R. L. Malenfant, *Adv. Mater.*, 2002, **14**, 99.
- 3 T. W. Kelley, P. F. Baude, C. Gerlach, D. E. Ender, D. Muires, M. A. Haase, D. E. Vogel and S. D. Theiss, *Chem. Mater.*, 2004, **16**, 4413.
- 4 Y. M. Sun, Y. Q. Liu and D. B. Zhu, *J. Mater. Chem.*, 2005, **15**, 53.
- 5 S. Allard, M. Forster, B. Souharc, H. Thiem and U. Scherf, *Angew. Chem., Int. Ed.*, 2008, **47**, 4070.
- 6 M. Mas-Torrent and C. Rovira, *Chem. Soc. Rev.*, 2008, **37**, 827.
- 7 R. P. Ortiz, J. Casado, V. Hernandez, J. T. L. Navarrete, J. A. Letizia, M. A. Ratner, A. Facchetti and T. J. Marks, *Chem.–Eur. J.*, 2009, **15**, 5023.
- 8 S. R. Forrest, *Chem. Rev.*, 1997, **97**, 1793.
- 9 V. Coropceanu, J. Cornil, D. A. da Silva, Y. Olivier, R. Silbey and J. L. Bredas, *Chem. Rev.*, 2007, **107**, 926.
- 10 A. R. Murphy and J. M. J. Frechet, *Chem. Rev.*, 2007, **107**, 1066.
- 11 J. Zaumseil and H. Sirringhaus, *Chem. Rev.*, 2007, **107**, 1296.
- 12 A. J. Baca, J. H. Ahn, Y. G. Sun, M. A. Meitl, E. Menard, H. S. Kim, W. M. Choi, D. H. Kim, Y. Huang and J. A. Rogers, *Angew. Chem., Int. Ed.*, 2008, **47**, 5524.
- 13 C. D. Sheraw, L. Zhou, J. R. Huang, D. J. Gundlach, T. N. Jackson, M. G. Kane, I. G. Hill, M. S. Hammond, J. Campi, B. K. Greening, J. Francl and J. West, *Appl. Phys. Lett.*, 2002, **80**, 1088.
- 14 H. Klauk, M. Halik, U. Zschieschang, G. Schmid, W. Radlik and W. Weber, *J. Appl. Phys.*, 2002, **92**, 5259.
- 15 T. W. Kelley, L. D. Boardman, T. D. Dunbar, D. V. Muires, M. J. Pellerite and T. Y. P. Smith, *J. Phys. Chem. B*, 2003, **107**, 5877.
- 16 H. E. Katz, *Chem. Mater.*, 2004, **16**, 4748.
- 17 J. S. Moore, *Acc. Chem. Res.*, 1997, **30**, 402.
- 18 S. Hoyer, *J. Polym. Sci., Part A: Polym. Chem.*, 1999, **37**, 2685.
- 19 M. M. Haley, J. J. Pak and S. C. Brand, *Top. Curr. Chem.*, **201**, 81.
- 20 C. Grave and A. D. Schluter, *Eur. J. Org. Chem.*, 2002, 3075.
- 21 D. Zhao and J. S. Moore, *Chem. Commun.*, 2003, 807.
- 22 Y. Yamaguchi and Z. Yoshida, *Chem.–Eur. J.*, 2003, **9**, 5430.
- 23 S. Hoyer, *Chem.–Eur. J.*, 2004, **10**, 1320.
- 24 S. Hoyer, *Angew. Chem., Int. Ed.*, 2005, **44**, 3806.
- 25 W. Zhang and J. S. Moore, *Angew. Chem., Int. Ed.*, 2006, **45**, 4416.
- 26 I. Hisaki, M. Sonoda and Y. Tobe, *Eur. J. Org. Chem.*, 2006, 833.
- 27 A. Mishra, C. Q. Ma and P. Bauerle, *Chem. Rev.*, 2009, **109**, 1141.
- 28 P. Bauerle, *Adv. Mater.*, 1992, **4**, 102.
- 29 Y. Y. Noh, J. J. Kim, Y. Yoshida and K. Yase, *Adv. Mater.*, 2003, **15**, 699.
- 30 A. Dadvand, F. Cicoira, K. Y. Chernichenko, E. S. Balenkova, R. M. Osuna, F. Rosei, V. G. Nenajdenko and D. F. Perepichka, *Chem. Commun.*, 2008, 5354.
- 31 H. Xu, G. Yu, W. Xu, Y. Xu, G. L. Cui, D. Q. Zhang, Y. Q. Liu and D. B. Zhu, *Langmuir*, 2005, **21**, 5391.
- 32 H. Xu, Y. Wang, G. Yu, W. Xu, Y. B. Song, D. Q. Zhang, Y. Q. Liu and D. B. Zhu, *Chem. Phys. Lett.*, 2005, **414**, 369.
- 33 Y. B. Song, C. Di, X. D. Yang, S. P. Li, W. Xu, Y. Q. Liu, L. M. Yang, Z. G. Shuai, D. Q. Zhang and D. B. Zhu, *J. Am. Chem. Soc.*, 2007, **129**, 1470.
- 34 T. Y. Zhao, Z. M. Wei, Y. B. Song, W. Xu, W. P. Hu and D. B. Zhu, *J. Mater. Chem.*, 2007, **17**, 4377.
- 35 Y. B. Song, C. A. Di, Z. M. Wei, T. Y. Zhao, W. Xu, Y. Q. Liu, D. Q. Zhang and D. B. Zhu, *Chem.–Eur. J.*, 2008, **14**, 4731.
- 36 Y. M. Sun, L. Tan, S. D. Jiang, H. L. Qian, Z. H. Wang, D. W. Yan, C. G. Di, Y. Wang, W. P. Wu, G. Yu, S. K. Yan, C. R. Wang, W. P. Hu, Y. Q. Liu and D. B. Zhu, *J. Am. Chem. Soc.*, 2007, **129**, 1882.
- 37 L. Tan, L. Zhang, X. Jiang, X. D. Yang, L. J. Wang, Z. Wang, L. Q. Li, W. P. Hu, Z. G. Shuai, L. Li and D. B. Zhu, *Adv. Funct. Mater.*, 2009, **19**, 272.
- 38 M. Mas-Torrent, P. Hadley, S. T. Bromley, X. Ribas, J. Tarres, M. Mas, E. Molins, J. Veciana and C. Rovira, *J. Am. Chem. Soc.*, 2004, **126**, 8546.
- 39 J. H. Gao, L. Q. Li, Q. Meng, R. J. Li, H. Jiang, H. X. Li and W. P. Hu, *J. Mater. Chem.*, 2007, **17**, 1421.
- 40 K. Memminger, T. Oeser and T. J. J. Muller, *Org. Lett.*, 2008, **10**, 2797.
- 41 J. E. Mcmurry, *Chem. Rev.*, 1989, **89**, 1513.
- 42 Y. Nishide, H. Osuga, M. Saito, T. Aiba, Y. Inagaki, Y. Doge and K. Tanaka, *J. Org. Chem.*, 2007, **72**, 9141.
- 43 L. V. Dunkerton, B. C. Barot and A. Nigam, *J. Heterocycl. Chem.*, 1987, **24**, 749.
- 44 S. Kumar, *J. Chem. Soc. Perkin. T.*, 2001, **1**, 1018.
- 45 M. Thelakkat and H. W. Schmidt, *Adv. Mater.*, 1998, **10**, 219.
- 46 H. Meng, M. Bendikov, G. Mitchell, R. Helgeson, F. Wudl, Z. Bao, T. Siegrist, C. Kloc and C. H. Chen, *Adv. Mater.*, 2003, **15**, 1090.
- 47 X. D. Yang, Q. K. Li and Z. G. Shuai, *Nanotechnology*, 2007, 18.
- 48 V. Coropceanu, M. Malagoli, D. A. da Silva, N. E. Gruhn, T. G. Bill and J. L. Bredas, *Phys. Rev. Lett.*, 2002, 89.
- 49 P. F. Barbara, T. J. Meyer and M. A. Ratner, *J. Phys. Chem.*, 1996, **100**, 13148.
- 50 K. D. Demadis, C. M. Hartshorn and T. J. Meyer, *Chem. Rev.*, 2001, **101**, 2655.
- 51 J. L. Bredas, D. Beljonne, V. Coropceanu and J. Cornil, *Chem. Rev.*, 2004, **104**, 4971.
- 52 E. F. Valeev, V. Coropceanu, D. A. da Silva, S. Salman and J. L. Bredas, *J. Am. Chem. Soc.*, 2006, **128**, 9882.
- 53 C. Risko, V. Coropceanu, S. Barlow, V. Geskin, K. Schmidt, N. E. Gruhn, S. R. Marder and J. L. Bredas, *J. Phys. Chem. C*, 2008, **112**, 7959.
- 54 J. Bouchard, M. Belletete, G. Durocher and M. Leclerc, *Macromolecules*, 2003, **36**, 4624.
- 55 K. M. Omer, S. Y. Ku, K. T. Wong and A. J. Bard, *J. Am. Chem. Soc.*, 2009, **131**, 10733.
- 56 G. M. Sheldrick, *SHELXL-97, Program for the Solution and Refinement of Crystal Structures*, University of Göttingen, Göttingen, Germany, 1997.
- 57 C. Lee, W. Yang and R. G. Parr, *Phys. Rev. B*, 1988, **37**, 785.
- 58 A. D. Becke, *Phys. Rev. A: At., Mol., Opt. Phys.*, 1988, **38**, 3098.
- 59 A. D. Becke, *J. Chem. Phys.*, 1993, **98**, 1372.
- 60 M. J. Frisch, G. W. Trucks, H. B. Schlegel, G. E. Scuseria, M. A. Robb, J. R. Cheeseman, G. Scalmani, V. Barone, B. Mennucci, G. A. Petersson, H. Nakatsuji, M. Caricato, X. Li, H. P. Hratchian, A. F. Izmaylov, J. Bloino, G. Zheng, J. L. Sonnenberg, M. Hada, M. Ehara, K. Toyota, R. Fukuda, J. Hasegawa, M. Ishida, T. Nakajima, Y. Honda, O. Kitao, H. Nakai, T. Vreven, J. A. M. Jr., J. E. Peralta, F. Ogliaro, M. Bearpark, J. J. Heyd, E. Brothers, K. N. Kudin, V. N. Staroverov, R. Kobayashi, J. Normand, K. Raghavachari, A. Rendell, J. C. Burant, S. S. Iyengar, J. Tomasi, M. Cossi, N. Rega, J. M. Millam, M. Klene, J. E. Knox, J. B. Cross, V. Bakken, C. Adamo, J. Jaramillo, R. Gomperts, R. E. Stratmann, O. Yazyev, A. J. Austin, R. Cammi, C. Pomelli, J. W. Ochterski, R. L. Martin, K. Morokuma, V. G. Zakrzewski, G. A. Voth, P. Salvador, J. J. Dannenberg, S. Dapprich, A. D. Daniels, O. Farkas, J. B. Foresman, J. V. Ortiz, J. Cioslowski and D. J. Fox, Gaussian, Incorporated, Wallingford, CT, 2009.
- 61 M. A. Thompson, *Planaria Software*, LLC, Seattle, WA.
- 62 G. Kresse and J. Furthmüller, *Comput. Mater. Sci.*, 1996, **6**, 15.
- 63 Y. Wang and J. P. Perdew, *Phys. Rev. B: Condens. Matter*, 1991, **43**, 8911.